12

Fabrication, Characterization and Thermal Properties of Nanowires

Yang-Yuan Chen, Cheng-Lung Chen, Ping-Chung Lee and Min-Nan Ou
Institute of Physics, Academia Sinica, Taiwan

1. Introduction

The physical properties of nanomaterials are novel and completely different from those in conventional bulk materials. The new discovered properties of nanomaterials not only reflected in electronic transports but also exhibited in optics and magnetism. For past decades, intensive and broad studies on nanoscience and nanotechnology were initialized all over the world. Nanoparticles (or quantum dots) are the first candidate of nanomaterials for such a study. In past the most important findings in nanoparticles are phonon softening, electronic energy level splitting and red shift etc. However due to their small size and dispersed characteristic, only few limited applications have been developed, the examples are the quantum dots in matrix for opto-electronics, dispersed nanoparticles for drug carries and thermal therapy of cancers etc. For above reasons, the study of nanowires (NWs) stimulates a great interest in their fundamental scientific researches and potential applications. The size effects, in general, have two aspects: one is the Quantum Size Effect (QSE), which originates from the variation of electronic density-of-states in nanostructure. QSE can thus derive a drastic change of transport and thermodynamic properties from those of the bulks. In contrast to Quantum Size Effect (QSE), the physical properties changed due to vast surface atoms, grain boundaries and structural deficiency are categorized to Non-Quantum Size Effect (NQSE), with no doubt this also inevitably plays an important role in the novel properties of nanowires. For examples, thermal and electrical conductivity of nanowires are significantly reduced as a result of electron/phonon scatterings occurring at grain boundaries of nanoscale crystallization. One of the most important characteristics of nanowire is its substantial small thermal conductivity. Thus, from manipulated materials to low-dimensional nanowires, it provides an innovative strategy to improve heat-electricity conversion efficiency for thermoelectric materials.

In the content of this chapter, two main sections will be included, the first section is the fabrication and characterization of nanowires, and the second section is the measurement techniques and setups for Seebeck coefficient, electrical conductivity and thermal conductivity.

For nanowire fabrication, two categories of fabrication method will be included. The first category is called the Bottom-up method, in which the nanowires were formed self-assembly. The second category of nanowire fabrication is the Top-down method, in which many patterning and etching processes are required for forming individual nanowires.

After nanowires are fabricated, the details of morphology, microstructures and crystallization of nanowires will be characterized and analyzed by various instruments such as scanning electron microscope (SEM), transmission electron microscope (TEM), X-ray diffraction (XRD) and energy dispersive X-ray (EDX).

At the end of this chapter, the introduction to techniques of physical property measurements for Seebeck coefficient, electrical conductivity and thermal conductivity on either nanowires array or a single nanowire will be described thoroughly. Several examples mentioned in this chapter are related to thermoelectric nanowires, the reason is that manipulating and optimizing the thermoelectric properties for sustainable energy applications has become a main stream of nanowire researches. Thermoelectric materials (TE) can be used either as a power generator based on the Seebeck effect, or a thermo-cooler based on the Peltier effect. The efficiency of a thermoelectric material is evaluated by its dimensionless figure of merit, $ZT = \sigma S^2 T/\kappa$, where T, S, σ, and κ are respectively the absolute temperature, Seebeck coefficient, electrical conductivity, and thermal conductivity (Rowe, 1995). Accordingly, the low thermal conductivity is a crucial factor for a material being a superior TE material. In the past few decades, bismuth telluride, Bi_2Te_3, has been recognized as the best TE material with ZT~1 near 300 K (Tritt, 1999). However, to fit in future applications, further enhancement of ZT is essential for the next generation TE materials. In this respect, reduction of dimensionality is a seemingly viable approach. For example, size-dependent behavior on thermal transport in nanowires has been studied by Li and his co-workers (Li et al., 2003). They found that the thermal conductivity of nanowires is much lower than the bulk value, and suggested that heat conduction in confined systems seems to be greatly influenced by phonon–boundary scattering. The same principle also works on Bi_2Te_3/Sb_2Te_3 superlattice thin films reported by Venkatasubramanian et al (Venkatasubramanian et al., 2001). Such phonon-blocking and electron-transmitting phenomena are indeed helpful in enhancing ZT. Much higher values were even predicted theoretically by Hicks and Dresselhaus for nanowires, based on the change of electronic density-of-states and increased phonon surface scattering (Hicks & Dresselhaus, 1993).

2. Fabrications and characterizations of nanowires

In general, nanowire fabrication methods can be categorized to two types. The first one is called the Bottom-up method, in which the nanowires are formed by self-assembly (Self-Assembly Method, SAM). The nanowires grown in the nano-porous template of anodic alumina oxide (AAO) by chemical electrodeposition are belonged to this category. Another method of nanowire fabrication, which is very similar to chemical vapor deposition, will also be introduced. By this method nanowires can be grown from deposited film through thermal annealing based on the stress generated from thermal expansion mismatching between the film and its substrate. The second category of nanowire fabrication is named the Top-down method. This method involves a lot of patterning and etching processes such as Optical Lithography (OL), Electron Beam Lithography (EBL), and etching techniques. Nanowires of Bi, Bi_2Te_3, and Sb_2Te_3 fabricated by this method will be illustrated. The control parameters of the growing conditions for the composition, size (or diameter) and crystallization of nanowires will also be involved. After the section of nanowire fabrication, the details of morphology, microstructures and crystallization of nanowires characterized by SEM, TEM, XRD and EDX will be followed.

2.1 Electrodeposition techniques and Anodic Alumina oxide (AAO) for the fabrication of Fe, Ni, Bi_2Te_3, and Sb_2Te_3 nanowires

Preparation of Anodic Alumina oxide (AAO)

Electrodeposition is an economic processing for depositing thin films and nanostructures due to its low-cost setup, high-yield production, and low energy consumption. Its capability for generating multifarious and high aspect ratio features is another advantage. So far, the method has been widely applied in the microelectronic industry for interconnects and magnetic storage (Andricacos et al., 1998; Osaka, 1999). Furthermore, the electrodeposition of metallic or semiconducting materials into nanoporous membranes such as AAO is considered as a conceptually simple and alternative way to fabricate nanowires, as shown in Fig. 1. In contrast to other deposition methods like thermal evaporation or chemical vapor deposition, the growth of nanowires in this technique can start from the pore bottom and continues in the pore direction to form nanowires array and is rather promising in various device applications. The following sections simply review the preparations and characterizations of magnetic and thermoelectric nanowires.

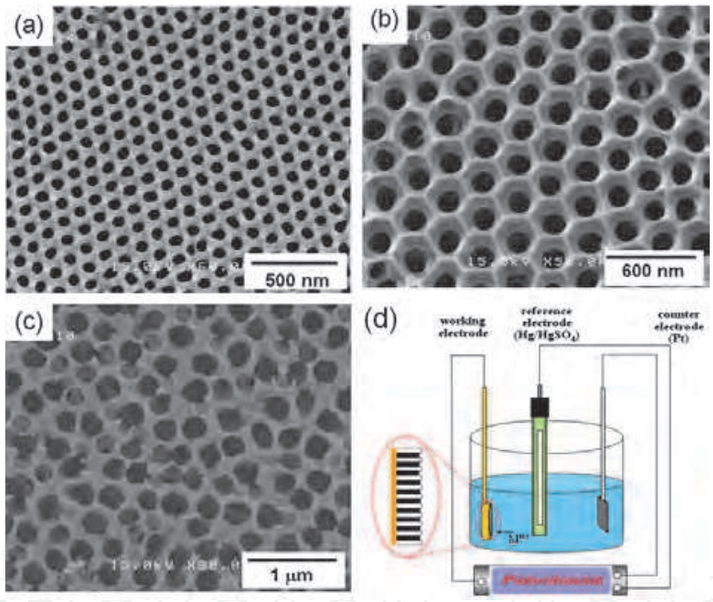

Fig. 1. Scanning electron micrographs of AAO templates with different pore sizes of approximately: (a) 60 nm, (b) 120 nm, (Reproduced with permission from Chen C. L. et al., *J. Phys. Chem.* C, 114, 3385-3389. Copyright ©2010 from American Chemical Society), (c) 200 nm, (d) The schematic arrangement of experimental electrodeposition setup. The deposition process is carried out in a conventional three-electrode cell with a saturated calomel electrode as the reference and a platinum sheet as the counter electrode. The AAO is attached to the working negative electrode for filling the chosen material through electrodeposition.

Fabrication of Fe and Ni nanowires in AAO templates

Nanostructured ferromagnetic materials are of interest in either theoretical studies or practical applications due to their anisotropic magnetism and magnetoresistance. These unique properties have great potential applications for high density magnetic storage

media, high sensitivity magnetic sensor and biologic technology (Liu et al., 1995; Reich et al., 2003). For example, perpendicular magnetic recording (PMR) of nanowires array could overcome the thermal instability limitation of superparamagnetism. Modern magnetic storage devices made by these materials can have bit densities in excess of 100 Gbit/in^2 (Weller & Moser, 1999). In preparation of Fe nanowires array, iron can be potentiostatically electrodeposited into a porous membrane by applying a voltage of -1.2 V, and the electrolyte solution consisting of $FeSO_4 \cdot 7H_2O$ (0.43 M) and boric acid (0.72 M) with pH~3 at room temperature (Ou et al., 2009). After the deposition, a mechanical polishing process was carried out to remove the overgrown thick iron layer on the top surface of AAO. The shinny surface on the top of iron nanowires array indicates that the oxidation of the materials is negligible. Subsequently, an electrodeposition of gold is performed to form a thin layer on the surface of the nanowire arrays to protect NWs from oxidation and serves as the contact electrode for electrical resistivity measurement. Fig. 2 shows the X-ray diffraction, morphologies, and structures of iron-filled nanowires array (Ou et al., 2009). The diffraction peaks of deposited films and 200 nm- nanowires array can be identified to be the (110), (200), and (211) planes of α-Fe; whereas 60 nm- Fe nanowires array shows a strong preferred orientation along the [110].

Besides the finite growth space has an obvious influence on the crystalline structures of nanowires, the magnetic properties of Fe nanowires array also greatly depend on the diameter of nanowires. The hysteresis loops for the Fe nanowires array with different sizes at 300 K are shown in Fig. 3. It is clear that 60 nm- Fe nanowire array shows a relatively strong hysteresis and anisotropic behavior than that of 200 nm- nanowires array. This intriguing feature can be attributed to the fact that the magnetic easy axis is along the longitudinal direction of nanowires, and which probably derives from the line shape anisotropy in nanowires.

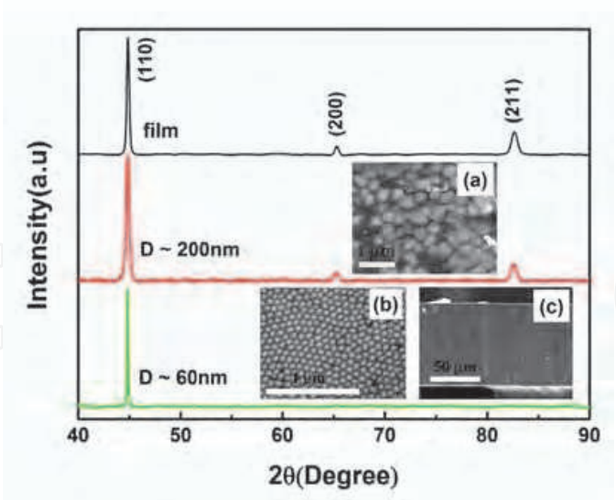

Fig. 2. X-ray diffraction patterns of the electrodeposited film, 200 nm-, and 60 nm-nanowires array. Insets (a) and (b) are the top views of the 200 nm- and 60 nm- nanowires, respectively. In these two images, white spots represent the alpha-Fe phase nanowires embedded in the template. (c) Side view of the home-made empty template (Reproduced with permission from Ou M. N. et al., *Chin. J. Phys.*, 47, 848-853. Copyright ©2009 from PSROC).

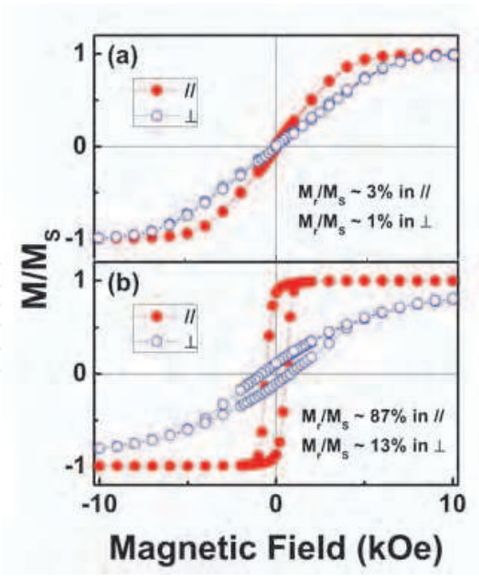

Fig. 3. Hysteresis loops of the Fe nanowires array with applied magnetic field parallel (∥) and perpendicular (⊥) to the longitudinal axis of the nanowires array: (a) 200 nm- and (b) 60 nm- NWs. The coercive fields in the easy axis are ~100 Oe and ~600 Oe for the 200 nm- and 60 nm- NWs, respectively. The ratios of the remanence (Mr) to the saturation magnetization (Ms) for different orientations are also presented. (Reproduced with permission from Ou M. N. et al., *Chin. J. Phys.*, 47, 848-853. Copyright ©2009 from PSROC).

Fabrication of Bi_2Te_3 and Sb_2Te_3 nanowires in AAO templates

Bi_2Te_3 is a narrow band gap semiconductor with an energy band gap of about 0.18 eV at 300K, and which can be either n- or p-type depending on the doping (Rowe, 1995). The electrodeposition of Bi_2Te_3 nanowires is mostly performed in nitric acid baths. The deposited crystal structures and their correlating compositions are highly dependent on the deposition potential, temperature, and the electrolyte concentration (Michel et al., 2006). In this respect, Martin-Gonzalez et al. proposed a Pourbaix-type diagram for the electrodeposition of Bi, Te, and their related deposits, and showed the thermodynamic stability of the dominant species as a function of pH value and potentials (Martıin-Gonzalez et al., 2002). As the deposited potential is altered to more negative value, Bi-rich deposits are obtained. Detailed investigations on the cyclic voltammetry of Bi, Te, and Bi/Te dissolved in 1 M HNO_3 revealed two different underlying processes. First process involves the reduction of $HTeO_2^+$ to Te^0 and forming Bi_2Te_3 through a subsequent interaction between Bi^{3+} and reduced Te^0. The second process occurring at more negative reduction potentials involves reduction of $HTeO_2^+$ to H_2Te followed by the chemical interaction with Bi^{3+}. The crystalline Bi_2Te_3 probably resulted from these two processes. This work indeed offers insights into the deposited mechanism of Bi_2Te_3. The overall chemical reaction can be described as:

$$2\ Bi^{3+} + 3\ HTeO_2^+ + 9\ H^+ + 18\ e^- \rightarrow Bi_2Te_{3(s)} + 6\ H_2O \quad (1)$$

According to the above conclusions, a series of Bi_2Te_3 nanowires were electrodeposited potentiostatically at -150 mV by filling nanoporous membrane in 1 M HNO_3 solution containing different Bi/ Te ratio to find the optimal deposition condition (Chen et al., 2010). These deposits were thus characterized by measuring their corresponding Seebeck

coefficients. Interestingly, all nanowires were *n*-type, and the optimal condition is about 0.008 M [Bi^{3+}] and 0.014 M [$HTeO_2^+$], corresponding to 65 μV/K. Once deviated from this electrolyte concentration, the measured Seebeck coefficients of the nanowires decrease to very small values. This event is understandable from the plot of Seebeck coefficient versus composition percentage for bulk Bi_2Te_3 (Rowe, 1995). Therefore, this parameter was selected for the preparation of Bi_2Te_3 nanowires. Through filling different sizes of template, the Bi_2Te_3 nanowires array with different diameter were fabricated, shown in Fig. 4. The filling ratio of these templates is higher than 80 %, and comparable to the best samples of this kind ever reported (Borca-Tasciuc et al., 2004). Judging from EDX analysis, only elements present in these nanowires are Bi and Te— in the ratio of 0.37± 0.02/ 0.63 ±0.03 corresponding to Te-rich *n*-type Bi_2Te_3. Extra Te may be situated as substitution to Bi sites or at interstitial sites. They may also be in grain boundaries, but not enough to be observed in XRD as impurity phase (Chen et al., 2010). Meanwhile, all the XRD patterns of these nanowires array can be indexed to rhombohedral structure, and confirming their single-phase purity. The strong (110) peak also suggests that the wires are highly textured in the [110] direction. This conclusion can be verified by the high-resolution transmission electron microscopy (HRTEM) result, shown in Fig. 5(b). In our experience, although annealing process can lower electrical resistivity of as-prepared film as expected, the annealing-induced thermal shock seems to have critical influence on the continuity of nanowires and leads to extremely high electrical resistance in nanowires embedded in AAO.

As for antimony telluride (Sb_2Te_3), it has the same crystal structure as Bi_2Te_3 with Sb atoms occupying Bi lattice sites. However, only a few efforts have been conducted on the electrodeposition of Sb_2Te_3 films and nanowires due to obstacles in the preparations of electrolytes. Recently, some limited studies have been reported. For example, Leimkuhler *et al*. developed an electroplating process for Sb_2Te_3 thin films on an indium tin oxide (ITO) substrate from an acid solution containing SbO^+ and $HTeO_2^+$ ions. In their investigations, the pH value, bath temperature, deposited potential, and composition ratio of the electrolyte significantly influenced the crystal structure and morphology of the film (Leimkuhler et al., 2002). Through controlling Sb/Te ratio in the electrolyte, the deposit composition could be adjusted to stoichiometry. Later, Jin et al. used a simple direct current electrodeposition process to synthesize Sb_2Te_3 nanowire array embedded in alumina templates (Jin et al., 2005). These conclusions demonstrate the possibility in electrodepositing Sb_2Te_3 films and nanowires; however, there is a lack of systematic studies for characterizing the physical properties of the deposits. According to the above conclusions, Sb_2Te_3 films were electrodeposited potentiostatically at -500 mV onto an ITO glass substrate from 1 M HNO_3 solution containing different Sb/ Te ratios (at 5~8 ^oC). In order to obtain well dissolved $SbCl_3$ in aqueous solution, 0.3 M of sodium citrate/ citric acid are suggested, which acting as complexing agents for Sb(III) ions (Huang et al., 2008). A conventional three-electrode cell was used for potentiostatic electrodeposition at room temperature. A platinum sheet was used as the counter electrode and a saturated calomel electrode (SCE) as reference. The working electrode is an ITO substrate, for the growth of films. In such condition, Sb and Te were in the form of SbO^+ and $HTeO_2^+$, respectively. The chemical reaction of these cations is described as (Leimkuhler et al., 2002):

$$2\,SbO^+ + 3\,HTeO_2^+ + 13\,H^+ + 18\,e^- \rightarrow Sb_2Te_3 + 8\,H_2O \quad (2)$$

With regard to the growth of Sb_2Te_3 nanowires, the working electrode was changed to AAO template, on which the evaporated gold/chromium (3000 Å/100 Å thick) film served as the

conducting layer. The nanowire arrays were synthesized via filling the AAO template under similar growth condition. Since the crystallization temperature of Sb_2Te_3 is slightly above room temperature (Huang et al., 2008; Baily & Emin, 2006), it is easy to prepare crystallized near stoichiometric Sb_2Te_3 nanowires by post-annealing treatment at 500 K in high vacuum (2×10^{-6} torr) for several hours. Figs. 6(b) and (e) are mechanically polished top view of AAO templates after being deposited with Sb_2Te_3. Obviously, the filling ratio can be higher than 80 %, and the elements present in the nanowires are Sb and Te— in the ratio of 0.39 ±0.02/ 0.61 ±0.03, corresponding to nearly stoichiometric Sb_2Te_3. The TEM images of 60 nm- Sb_2Te_3 nanowire are given in Figs. 5(c) and (d). From Fig. 6(g), most XRD peaks of these nanowires can be indexed to rhombohedral structure (standard ICCD PDF card 71-0393); however, the peak marked with an asterisk is indexed to a $Sb_{0.405}Te_{0.595}$ structure (monoclinic, ICCD PDF card 45-1229). That means the crystal structures of the prepared nanowires probably contained two phases: rhombohedral and monoclinic.

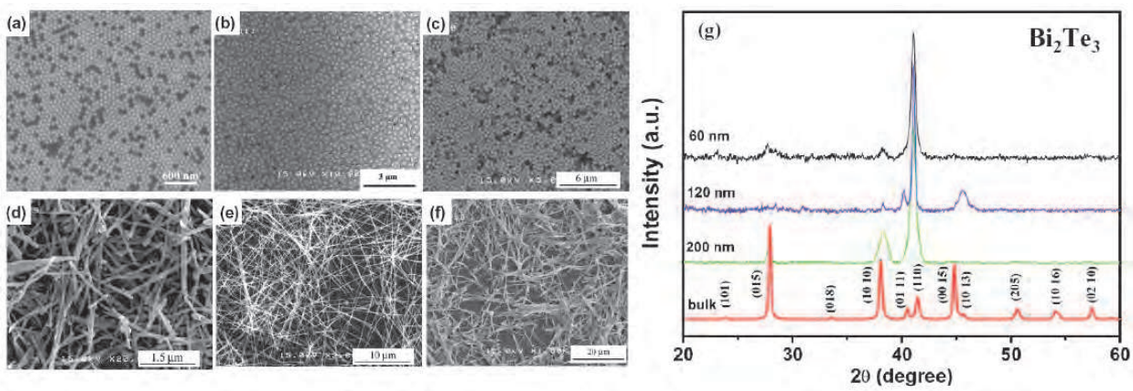

Fig. 4. SEM micrographs and XRD patterns of Bi_2T_3 nanowires array. Surface view: (a) 60 nm, (b) 120 nm, (c) 200 nm. Separated nanowires after AAO being dissolved: (d) 60 nm, (e) 120 nm, (e) 200 nm. (g) XRD patterns of Bi_2Te_3 bulk, and as-prepared nanowire array of different diameters (60, 120, and 200 nm). (Reproduced with permission from Chen C. L. et al., *J. Phys. Chem.* C, 114, 3385-3389. Copyright ©2010 from American Chemical Society).

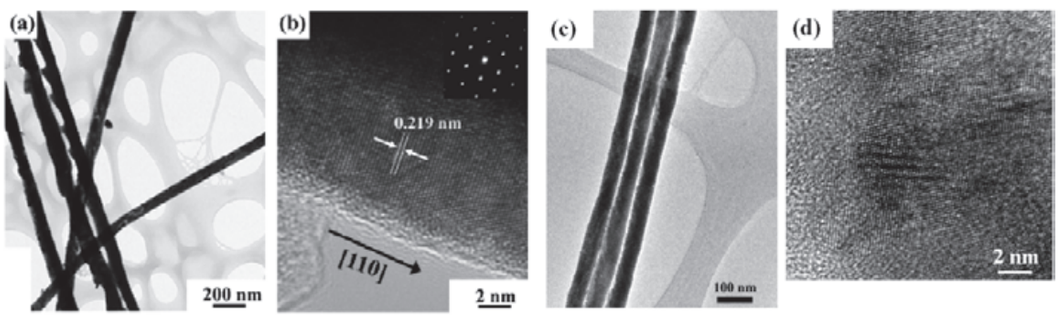

Fig. 5. TEM images of Bi_2Te_3 and Sb_2Te_3 nanowires. (a) The uniform profile of Bi_2Te_3 nanowires with a diameter of 120 nm. (b) HRTEM image of a single Bi_2Te_3 nanowire. Inset: Diffraction patterns of a selected area. (c) TEM images of Sb_2Te_3 nanowires with a diameter of 60 nm. (d) High resolution image of a single Sb_2Te_3 nanowire. (Reproduced with permission from Chen C. L. et al., *J. Phys. Chem.* C, 114, 3385-3389. Copyright ©2010 from American Chemical Society).

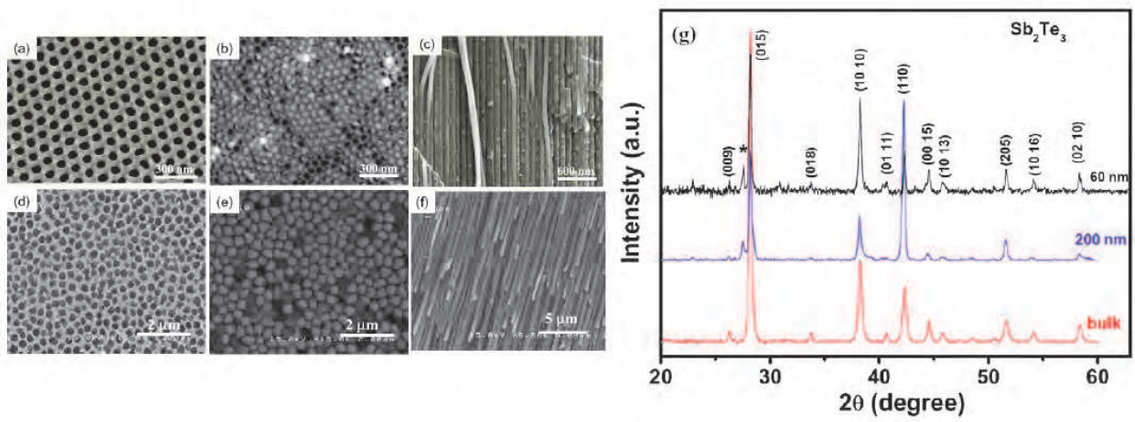

Fig. 6. SEM micrographs and XRD patterns of Sb_2T_3 nanowires array. Top view images: (a) to (c) d~ 60 nm; (d) to (f) d~ 200 nm. Figures (c) and (f) are cross-sectional views, and the others are surface views. (g) XRD patterns for Sb_2Te_3 bulk and nanowires array of different diameters. The peak marked with an asterisk is indexed to a $Sb_{0.405}Te_{0.595}$ structure (monoclinic, ICCD PDF card 45-1229).

2.2 Fabrication of Bi, Bi_2Te_3 nanowires by stress-induced method

More recently, Shim and Ham *et al.* (Shim et al., 2009; Ham et al., 2009) proposed the fabrication of single crystalline Bi and Bi_2Te_3 NWs based on a mechanism in which the mismatch of the thermal expansion between the substrate and the film can drive the mass flow along grain boundaries to grow nanowires during thermal annealing temperature. Such growth process of nanowires is a kind of releasing the compressive stress by means of atomic diffusion. Although the inspiration of this interesting growth idea of the author comes from the formation of whiskers or hillocks in metal films (Au, Sn, Zn, In) in electronic packaging process, in fact this mechanism is entirely different from the above (Tu, 1996). In a typical procedure, the chosen material is initially deposited onto a thermally oxidized silicon substrate. Then the film is heated up to optimal annealing temperature, for example, 270 ^oC for Bi, and 350 ^oC for Bi_2Te_3. The length of nanowire is proportional to the annealing time, and the diameter of the wire is tunable by controlling the mean grain size of the deposited film. In the case of Bi nanowires, the nanowires were found to grow along the [001] direction, and was defect-free, single crystalline. The relationship between growth direction of nanowires and orientations of grains in the film is not clear. Interestingly, the Bi_2Te_3 nanowires can be also grown by the same mechanism to exhibit single crystallinity with growth direction along [110], and the chemical composition of the nanowire is close to stoichiometry. To further understand the thermoelectric properties of nanowires prepared by following method, we have followed the same growth mechanism to prepare Bi_2Te_3 nanowires, and successfully obtained the single crystalline nanowires, shown in Fig. 7. The detailed electrical and thermoelectric properties will be discussed in the next section. The development of this method definitely provides researchers an alternative route to prepare nanowires, and also promotes the application possibility by utilizing Bi and Bi_2Te_3 nanowires in thermoelectric devices.

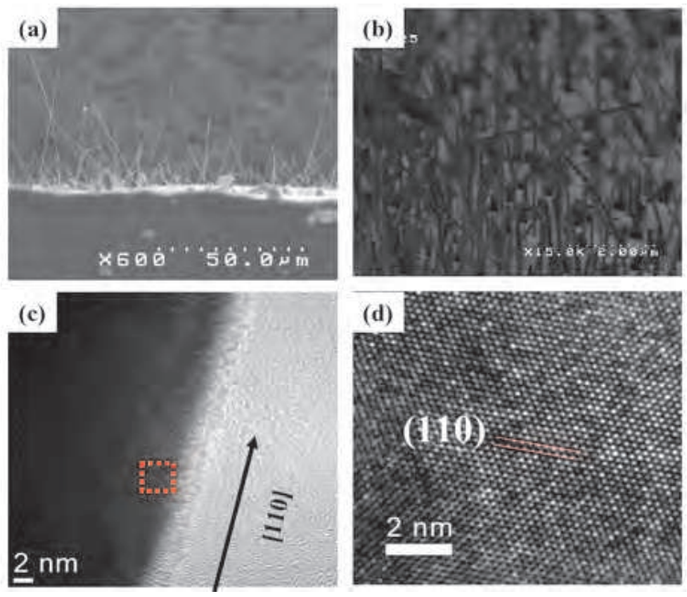

Fig. 7. SEM and TEM images of the prepared Bi_2Te_3 nanowires. (a) The side view image clearly shows that all nanowires grow from the surface of the deposited film. (b) The image reveals very dense and uniform nanowires with several micrometers in length. (c) A low-magnification TEM image of a Bi_2Te_3 nanowire, and (d) A HRTEM image taken from selected area marked in (c) of the Bi_2Te_3 nanowire indicates that the growth direction of the nanowire is [110].

2.3 Fabrication of individual nanowires of Ni, Bi_2Te_3 and Sb_2Te_3 using lithographically patterned method

Lithography

In general, the lithography is a series of processes of photoresist coating, e-beam writing or mask-light exposure and photoresist removing. The series of progresses can be repeated many times and depend on the complexity of the pattern designed. We defined a pattern by transfer a predesigned pattern with an energetic source in a moveable photoresist layer, then remove the useless parts of the pattern by various etching techniques. Typically, the energetic source can be a light beam or electron beam, which used to transfer predesigned patterns by either projecting or masking to define a two-dimensional shape for devices over an entire surface simultaneously. The pattern formed by this method is named optical or electron-beam lithography that is up to the kind of beam source adapted. The remaining parts of photoresist would be a protecting layer for etching process.

Optical lithography (OL) and Electron Beam Lithography (EBL)

Optical lithography is also called Photolithography is a process to remove parts of a thin film. Usually, it applies ultraviolet light to transfer a pattern from a mask to a light-sensitive photoresist on the substrate. The processes are consisting of wafer cleaning, baking, exposure and development. The schematic steps are shown in figure 8 for a typical pattern on a silicon substrate. After Si substrate is cleaned, a uniform metal layer is deposited on it, and followed by a subsequent photoresist coating. Only the selected parts defined by a patterned mask are exposed to illumination of ultraviolet light, the photoresist exposed to

illumination can be easily removed in developer bath. In principle, the resolution can be increased by using shorter wavelengths such as X-ray. Instead of light illumination, electron beam may be used for electron resist, like PMMA (poly-methyl metacrylate). For positive resist, the electron beam breaks the bonds between the monomers with increased solubility results. For negative photoresist, on the other hand, the electron beam generates inter-chain cross linking and decreases its solubility. For EBL, a focused electron beam is scanned in a predefined pattern. In contrast to optical lithography one time exposure of illumination, this is a much slower process. However the structure with size resolution smaller than 50 nm can be made. Using high energy electron beam, usually larger than 30 keV, an extremely small spot of about 1 nm can be achieved. However the expose resolution is much worse than spot size of electron beam, the backscattered secondary electrons from the substrate actually expand the exposure size of resist. The secondary exposure to the resist causes an undercut profile. The undercut is often improved by coating a two-layer electron beam resist. By these techniques, the various materials like nickel, $BiTe_x$, and $SbTe_x$ were produced successfully with the wire size around 100 nm, as shown in Figs. 8 (c), (d), and (e). In principle, the find tune of e-beam exposure could reduce the width of wire-like pattern down to 30 nm.

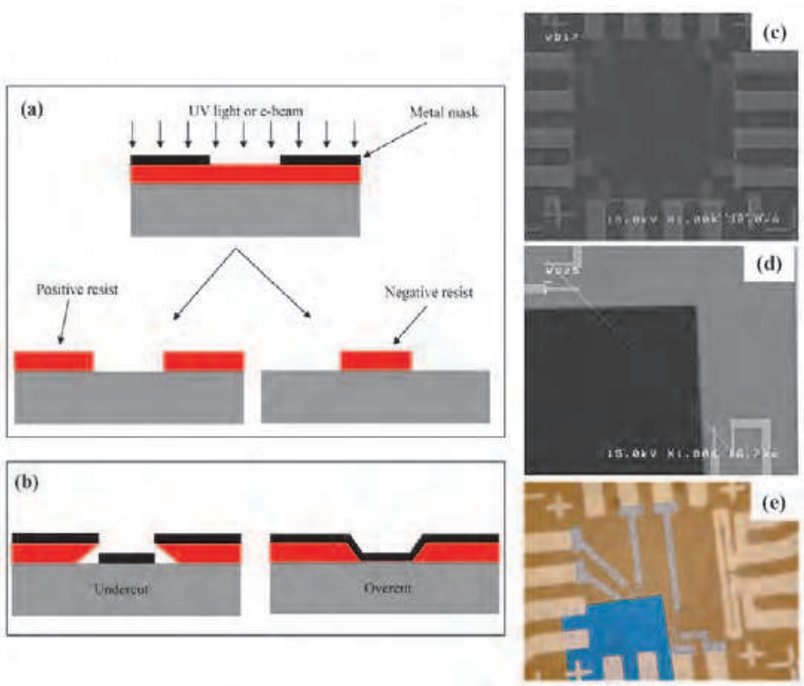

Fig. 8. The selected resists and exposure devices may change the pattern resolution by the typical sequences of process steps. (a) The resist cross section of positive and negative resist. The solubility of the exposed areas increases for a positive resist while it decreases in negative resist. (b) The resist profile of different resists. (c), (d), and (e) are micrographs of nickel, $BiTe_x$, and $SbTe_x$ nanowires, respectively.

Fabricating a sagging nickel nanowire

The details of optical and e-beam lithography methods are described below. The key steps of fabrication process for the sagging single nickel nanowire (Ni-NW) are shown in Fig. 9(a).

(Ou et al., 2008). In order to measure thermal conductivity and specific heat of an individual nanowire by 3ω method which will be described below, there are some requisitions. With no doubt, the primary part of the wire should be separated from substract to minimize heat leakage in measurement. For example, the heat could leak to substrate and environments by direct heat-contact and radiation. Furthermore, the two ends of sample should have well thermal contact to substrate to satisfy the requirement that two ends of wire have same temperature as that of substrate. How to fabricate a sagging single nickel nanowire to meet the criterion mentioned above will be described below.

The primary substrate is p-type silicon wafer coated by a 200 nm thickness silicon-nitride (Si_3N_4/Si) with [100] out-plane orientation. Meanwhile, a photoresist layer was uniformly deposited to protect the silicon under silicon-nitride from the etching of KOH aqua. The desired pattern was defined with focused electron beam (E-Beam) on a clear and polymethyl methacrylate (PMMA)-coated primitive chip. This pattern includes four wires for four-probe measurement. The configuration of the chip is consist of one nano-ditch, two thin leads for signal pick up and two wide leads for current injection. The designed nano-ditch is 35 μm in length and 150 nm in width (Fig. 9(b)). To minimize the joule heating generated at the interfaces and current leads, the width of leading wires are about 50 times of the nano-ditch. Furthermore, also the nano-ditch takes about 8 μm away from the junction to reduce the temperature fluctuation at the two end parts of nanowire.

In the next step, a 100 nm thickness film of nickel was deposited on the exposed and developed chip by thermal evaporator in vacuum chamber with a base pressure less than 1×10^{-6} torr. The followed lift-off process would take off the resist and the nickel above. Finally a single Ni nanowire with four electrodes was fabricated. The resistance of the nanowire was measured by four-probe method with resistance about 750 Ω. This patterning process was repeated again to form an etching window allowing CF_4 to etch out the Si_3N_4 with a "V" shape groove around the nanowire by reactive-ion etching (RIE) (Fig. 9(b)). The formed sagging nickel nanowire is about 35 μm in length and 180 nm in width, shown in Figs. 10(a), (b), and (c). This junction-free nanowire with lead electrodes prevents undesired heating at joints during measurements. Although this sample went through all the measurements processes, its resistance is kept around 750 Ω. This consequence implies that the stability of the specimen with no visible surface oxidation.

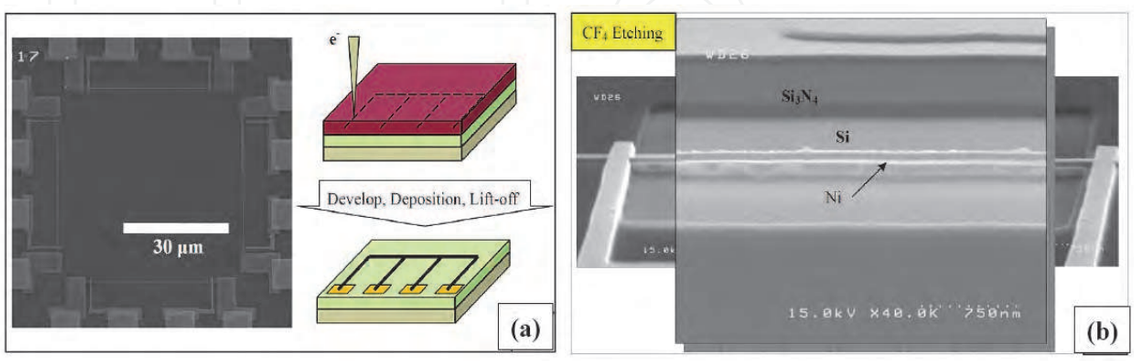

Fig. 9. The defined pattern and etching results. Inset (a) shows the sequence of e-beam exposure, developed and deposition, and lift-off. Inset (b) shows the magnification of the single nanowire.

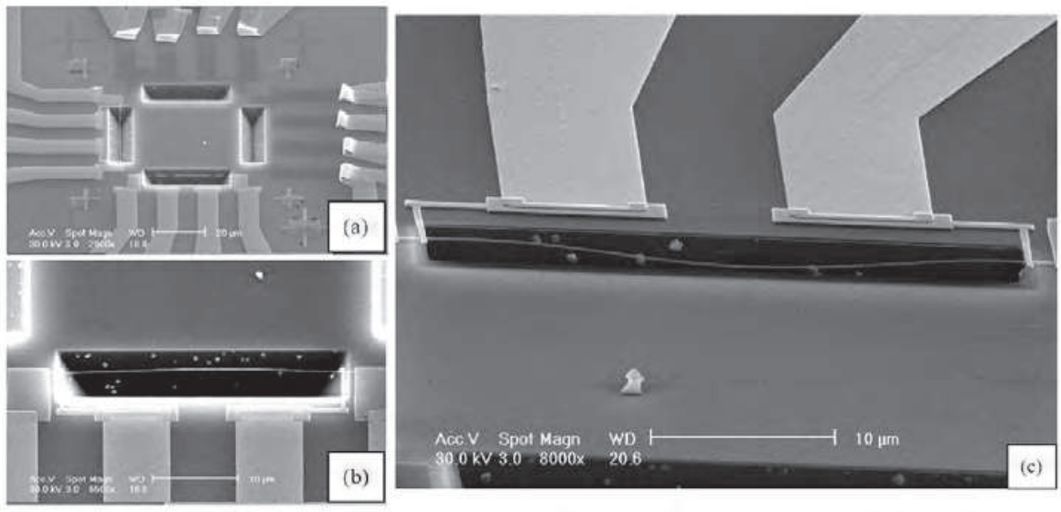

Fig. 10. The SEM images of the sagging Ni-NW. Inset (a) and (b) are the top view with different magnifications. Inset (c) is the image with 45 degree tilt angle. (Reproduced with permission from Ou M. N. et al., *Appl. Phys. Lett*., 92, 063101-063103. Copyright ©2008 from American Institute of Physics).

3. Measurement techniques of transport and thermal properties

In this section, the techniques for measurements of Seebeck coefficient, electrical conductivity and thermal conductivity for either nanowires array or a single nanowire will be illustrated thoroughly. Basically the measurement techniques for physical properties of nanowire are very similar to those for bulk, except a couple of issues which have to be taken into account in the measurements for nanoscale specimens. The first one is how to place or prepare the nanowire sample in a measurement platform; the second one is how to narrow down the size of measurement probes and their configuration which is comparable to the size of nanowire. For nanowires array sample, like AAO templates, their sizes are usually down to a few to a hundred micrometers that are in the same order as measuring probes and lead contacts, for example, thermocouple dips and electrodes respectively. To obtain correct result, reducing the size of the measurement probes and their contacts are inevitable. For measurement of a single nanowire, there are a couple of tools available to solve the problem. Below, we demonstrate the procedures for nanowire array measurement and two approaches to prepare and measure a single nanowire specimen.

3.1 Measurement principle and setup

Measurement platform fabrication for nanowires array

A longitudinal DC steady-state set-up for bulk specimens is employed to measure the temperature gradient, ΔT, and generated thermo-emf (EMF), ΔV, across the nanowire specimen and thus the derivation of the Seebeck coefficient S (= $\Delta V/\Delta T$). Two pairs of thermocouples with 25 µm diameter were served as the temperature probe and electric leading wires for EMF measurement. The silver paste is used to assist better thermal and electrical contact. The four wires of thermocouples can also be employed for electrical conductivity measurement of semi-four probe method. The schematic setup is shown in Fig.

11 (Chen et al., 2010). For thermal conductivity measurements, as the specimen size is larger than 6 mm in diameter, then it generally can be accomplished using laser flash setup of thermal diffusivity and calorimeter of specific heat.

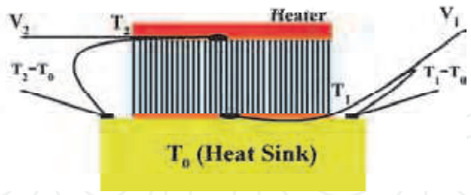

Fig. 11. Schematic setup for Seebeck coefficient measurements on nanowires array of AAO. (Reproduced with permission from Chen C. L. et al., *J. Phys. Chem.* C, 114, 3385-3389. Copyright ©2010 from American Chemical Society).

Measurement platform fabrication for a single nanowire

The method is to transfer a pre-fabricated nanowire to a silicon wafer which will be further processed to a measurement platform using lithography procedures. There are a couple of methods to achieve this goal. One is by directly attaching the sample substrate, on which nanowires were grown, to a blank silicon wafer (Fig. 12). Or alternatively, you can dip a drop of liquid containing nanowires to the silicon wafer.

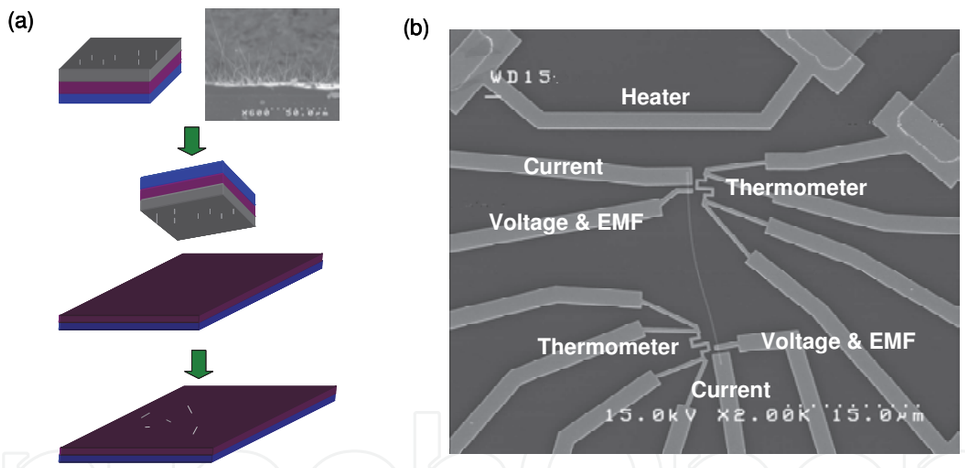

Fig. 12. (a) The processes of transferring nanowires to the working silicon wafer. (b) The SEM picture of a Bi_2Te_3 nanowire specimen and configuration of electrical leads, heaters and temperature thermometers.

For more precise sample control and manipulation, four nano-manipulation probes integrated into an SEM can be employed to select and pick up a nanowire and lay it down to a specific region of a well prepared template (Fig. 13(a)). This template has a SiN_x membrance in the center with underneath been etched away. After nanowire was placed, EDX and SEM were applied to analyze the configuration and morphology of the nanowire, and mark the position of nanowire simultaneously. Followed by photolithograph and e-beam lithography processes, patterning of leading wires, thermometers and heaters can be accomplished. For suspending the nanowire, the SiN_x membrane can be removed by various etching processes. Now the suspended nanowire is ready for all kinds of measurements of Seebeck coefficient, electrical conductivity and thermal conductivity (Fig. 13(b)).

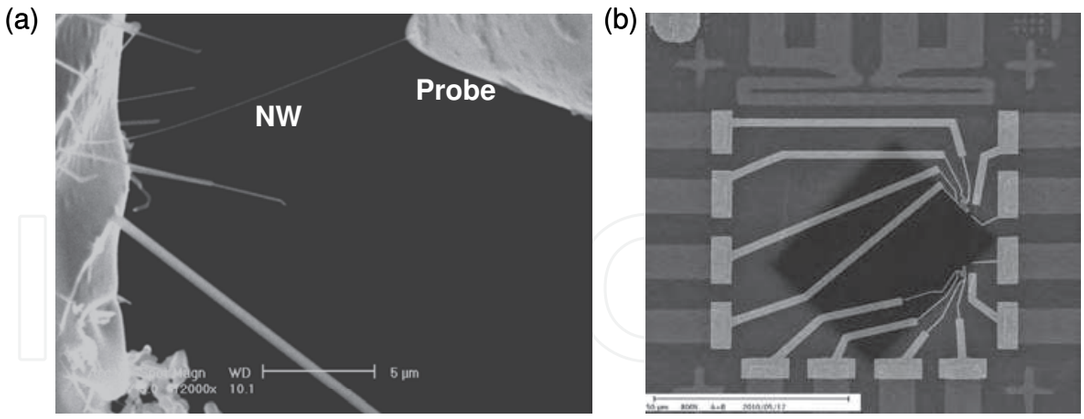

Fig. 13. (a) Shows the controllable probe in SEM attached a Bi_2Te_3 nanowire grown on the silicon substrate. (b) The SEM picture of the measurement platform for Bi_2Te_3 nanowire sample.

3.2 Measurements of Seebeck coefficient

The Seebeck coefficient (S) is defined as:

$$S = -\frac{\Delta V}{\Delta T} \tag{3}$$

ΔT is the temperature gradient of the sample, and ΔV is the generated EMF. A traditional Seebeck coefficient measurement setup for bulk sample is shown in Fig. 14(a). However for nanowire specimen, the setup and design are completely different, as shown in Fig. 14(b).

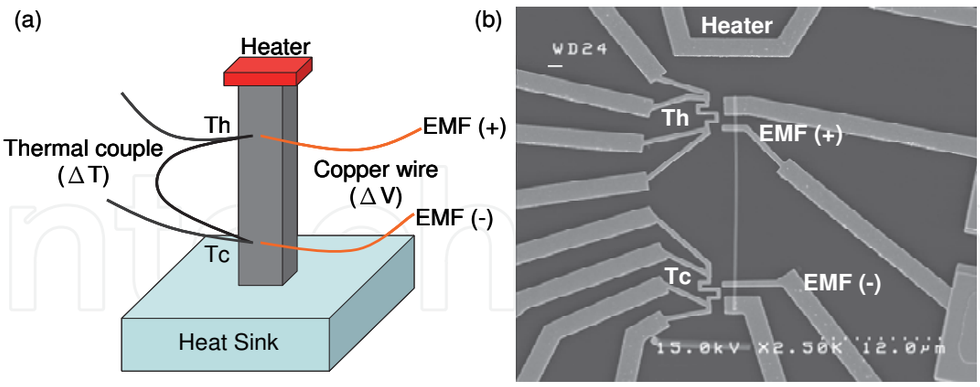

Fig. 14. (a) A traditional Seebeck coefficient measurement setup for bulk specimens. (b) The setup for a single Bi_2Te_3 nanowire specimen.

In Seebeck coefficient measurement, the main issue is how to reduce the measurement error of temperature gradient across the specimen. The error of temperature measurement mainly comes from two sources, the thermometer size and the non-common position of the thermometer and EMF probe. For bulk sample, in general, typical size of thermal couples is small enough for the pinpoint of the exact position of temperature measured. For nanowire measurement, the size of traditional thermocouples is no longer applicable in nanoscale. For

nanowire measurement, the resistive metal wires are served as thermometers but narrowed down to nanometer scale. In Fig. 15, an example measurement of Seebeck coefficient measurements for a Bi_2Te_3 nanowire at 180 K is shown. The Seebeck coefficient about -5 μV/K is obtained by the linear fit to the data of ΔV versus ΔT.

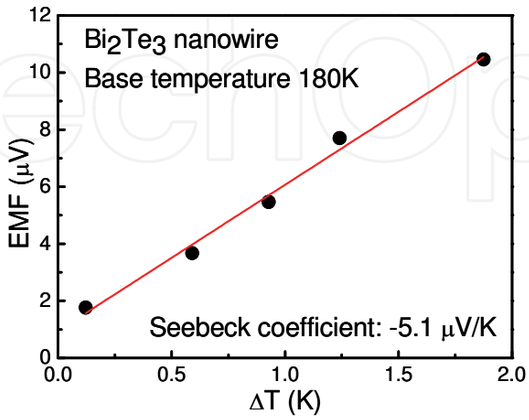

Fig. 15. The Seebeck coefficient measurement of a single Bi_2Te_3 nanowire at 180 K.

3.3 Measurements of electrical and thermal conductivities of a nanowire

Electrical conductivity measurements

The arrangement of measuring circuit diagram for electrical conductivity of Ni nanowire is shown in Fig. 16. An AC current was injected through two outside electrodes (L_5 and L_6), and voltage drop was picked up by two inner electrodes (L_2 and L_3). A measured current dependence of voltage is shown in Fig. 17. Within the current range from 1 to 50 μA, a linear dependence of voltage versus current is exhibited, indicating the resistivity of Ni nanowire follows Ohmic law. The measurement of electrical conductivity was excited by an alternating current described by a sine wave $I_0\sin(\omega t)$ with frequency f= 15.3 Hz. The corresponding in-phase voltage signal of the same frequency was picked up by a lock-in amplifier.

The data of resistivity ρ of the nickel nanowire (Ni-NW) in the temperature region of 0.5- 300 K is showed in Fig. 18. The temperature dependence of resistivity is metallic and similar to that of the bulk but with a larger magnitude of resistivity. The relative ratio of resistivity, $\rho(300\text{ K})/\rho(4.2\text{ K}) = 2$, is much smaller as compared to the value of 47 for the bulk. Since the wire dimensions are much larger than the mean free path of Ni (~14 nm) (Reale, 1974), the increase in resistivity is conjectured to be the predominant effect of the grain–boundary scattering. The temperature coefficient of resistivity (TCR) is positive in the entire temperature range, indicating that the Ni-NW is weakly disordered. At low temperatures T < 10 K, the temperature dependence of resistivity can be formulated as $\rho = \rho_0 + T^n$, with the power n ~ 2 (inset in Fig. 18). The consequence is similar to that of the bulk (Zhang et al., 2001), except the magnitude of residual resistivity ρ_0= 17.6 μΩ-cm is five times of bulk Ni. The huge residual resistivity indicates an enhanced electronic scattering on boundaries and defects.

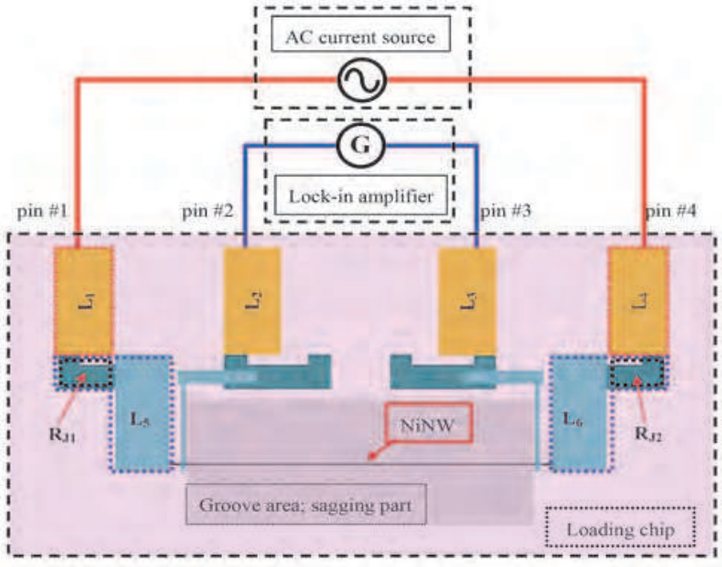

Fig. 16. The schematic diagram of the nanowire specimen and electrode leads for both electrical and thermal conductivity measurements. Nanowire (100 nm×180 nm×35 μm) and electrode pads were fabricated from a piece of thermally deposited Ni film using photolithography and e-beam writer, thus there is no junction between nanowire and electrode pads. L_1, L_2, L_3 and L_4 are the gold electrode pads.

It is noted that the ρ(T) curve of Ni-NW is well fitted to the modified Bloch-Gruneisen formula by Wilson (White & Wood, 1959) for transition metals with Debye temperature θ_D and constant d as the two adjustable fitting parameters. As a result of the fitting, we obtained the smaller value of θ_D = 440 K than that of the bulk (θ_D= 557 K) at fixed d. The reduction of the Debye temperature presumably reflects the phonon softening due to the enhanced disorders in nanowires. The consequence was previously observed in other nanowires and disordered systems (Bid et al., 2006; Fultz et al., 1997; Frase & Fultz, 1998).

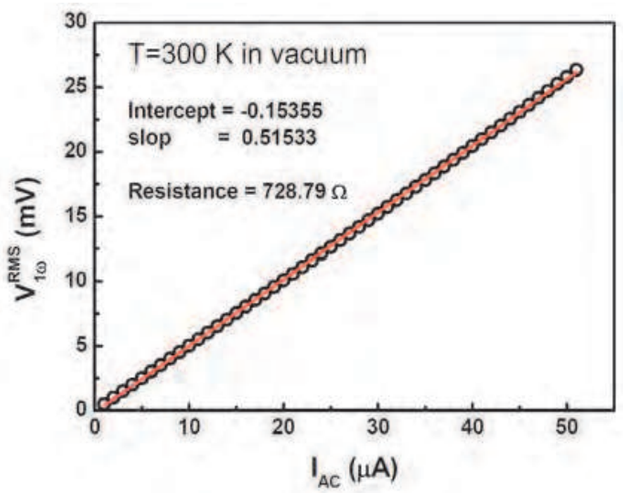

Fig. 17. The current dependence of voltage signal. Experimental data represented by open circles are fit to a solid line.

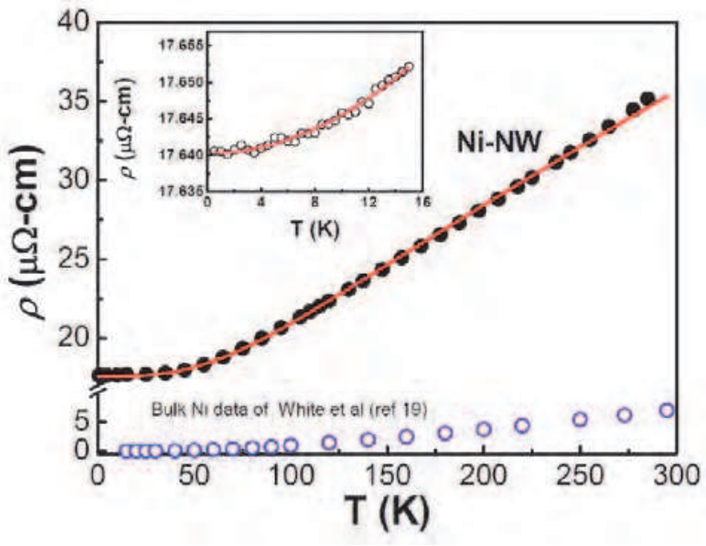

Fig. 18. The resistivity $\rho(T)$ of the Ni-NW (solid circles) and the bulk (open circles) from White et al. The solid line is the fitting results using Bloch-Gruneisen formula (Bid et al., 2006). The inset: the resistivity in low temperature range is in good agreement with the curve of T^2 dependence. (Reproduced with permission from Ou M. N. et al., *Appl. Phys. Lett.*, 92, 063101-063103. Copyright ©2008 from American Institute of Physics).

Specific heat, electrical and thermal conductivity measurements using 3ω method

Usually, the thermal conductivity κ(T), electrical conductivity σ(T), and specific heat C(T) are measured separately using different instruments. However, by 3ω method (Ou et al., 2008; Allwood et al., 2005; Lu et al., 2001; Ou et al., 2007), the three parameters can be measured on a specimen simultaneously. Although the nanowire still exhibits metallic behavior in ρ(T), the situation in thermal conductivity is changed drastically. The schematic diagrams of electrical connections are similar to the setup of resistance measurement. An example of thermal conductivity measurement is illustrated below.

To apply 3ω method for the measurement of sagging Ni-NW, a couple of restricted conditions have to be taken into account. In Fig. 16, the current path is consisting of current leads, junctions, and specimen, thus the total resistance of current loop can be represented by following formula:

$$R_t = R_{L1} + R_{J1} + R_{L2} + R_{Ni\text{-}NW} + R_{L3} + R_{J2} + R_{L4} \tag{4}$$

Since the mass ratio of leads to Ni-NW is about 10^5, the estimated power density of leads and junction is ignorable as compared to that of Ni-NW, this consequence satisfies the restriction conditions of 3ω method. A junction-free design has been made to prevent the measurement error which could be caused by unexpected temperature variation of electrical contacts.

The 3ω signal across specimen of the sagging Ni-NW is represented by following approximation solution:

$$V_{3\omega} \approx \frac{4I^3 LRR'}{\pi^4 \kappa S\sqrt{1+(2\omega\gamma)^2}}, \tag{5}$$

where the κ and γ are thermal conductivity and thermal time constant, respectively. To select appropriate ranges of frequency and magnitude of exciting current, a test run was performed at 300 K to ensure the condition of $V_{3\omega} \propto I^3$ is held (Fig. 19). For the signal picking- up, a digital lock-in amplifier was selected to pickup the 3ω signal of $V_{3\omega}$. To ensure the observation of a true frequency dependence of $V_{3\omega}$ the dc coupled input mode was selected with no filters was applied. In Fig. 20, the frequency dependencies of $V_{3\omega}$ signal at 15, 85, 155, 225, and 295 K are fitted to the theoretical predication (the solid lines) of Eq. 5 to derive the magnitudes of thermal conductivity κ.

The thermal conductivity κ in the temperature region of 15-300 K is shown in Fig. 21. Thermal conductivity monotonically decreases as temperature drops. The κ(T) of Ni-NW showed a completely different temperature dependent trend and is much smaller when compared with the bulk (inset of Fig. 21) (White & Wood, 1959). The phenomena of the metallic electrical resistivity and decreasing thermal conductivity have been observed in disordered metallic systems of thin films, concentrated alloys and superlattices (Zhou et al., 2006; Zhang et al., 2006; Yang et al., 2006; Berman, 1976). Such behavior was explained by increased scattering of heat carrier with the structural defects and by the substantial contribution of the phonon thermal conductivity. In general, thermal conductivity κ is the summation of electronic κ_E and phonon κ_{PH}. If the WF (Wiedemann Franz) law holds, one can obtain κ_E from the data of ρ(T) through the relation $\kappa_E = L_0 T/\rho$. The calculated κ_E for T< 60 K is larger than the experimental data κ_{total}, indicating the violation of the WF law in this temperature region. To estimate the phonon part of thermal conductivity κ_{PH} for T> 100 K, κ_E was subtracted from experimental κ_{total}; the result of κ_{PH} does not exceed 10 % of total thermal conductivity κ_{total}, and thus no considerable enhancement in the phonon part was observed at this temperature region.

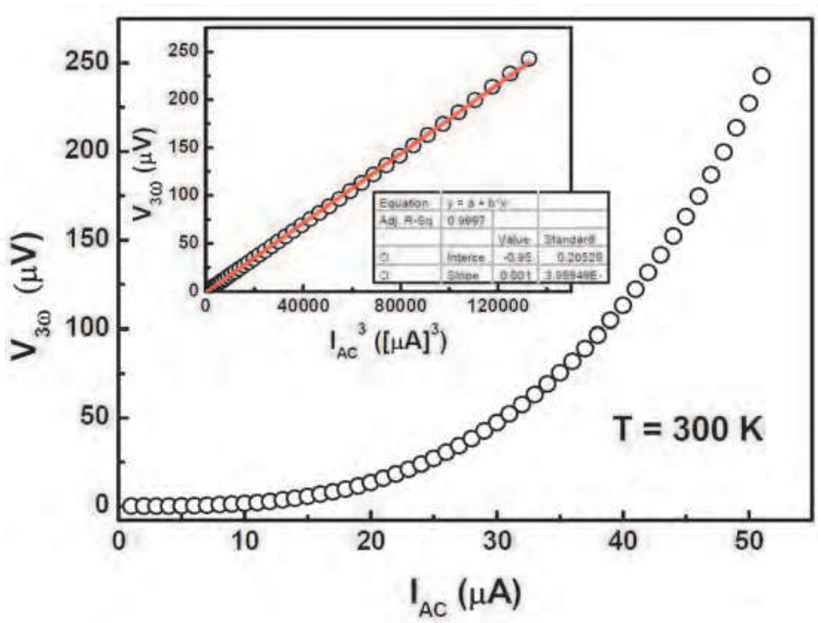

Fig. 19. The current dependence of 3rd harmonic signal at 300 K. The inset shows the linear dependence of $V_{3\omega}$ versus I^3.

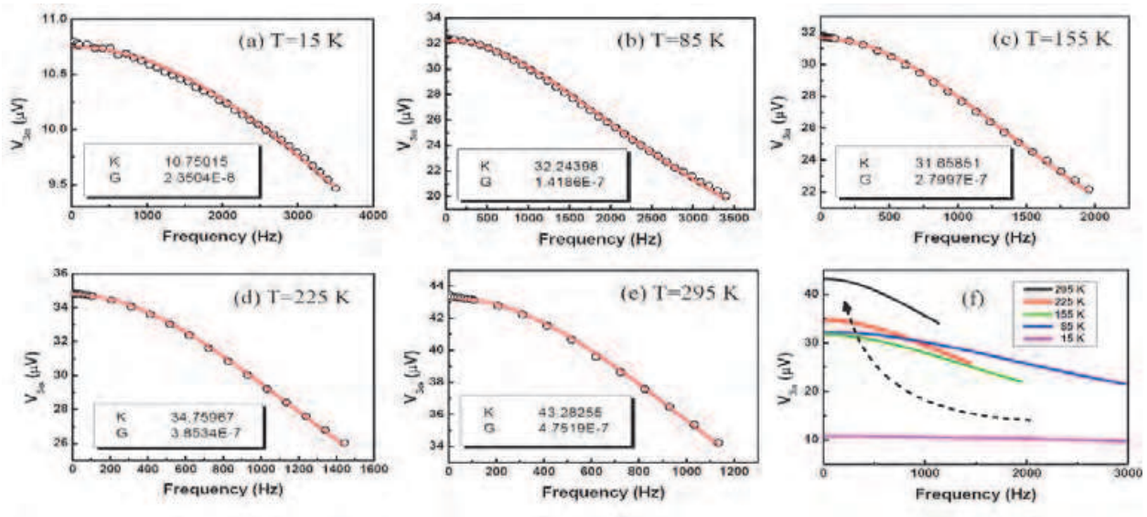

Fig. 20. The frequency dependence of 3rd harmonic signal. (a) to (e) are experimental data and curve fittings for the results of thermal conductivity κ. The frequency dependencies of $V_{3\omega}$ signal for different measurement temperatures are displayed in (f) to show the trend as temperature changes.

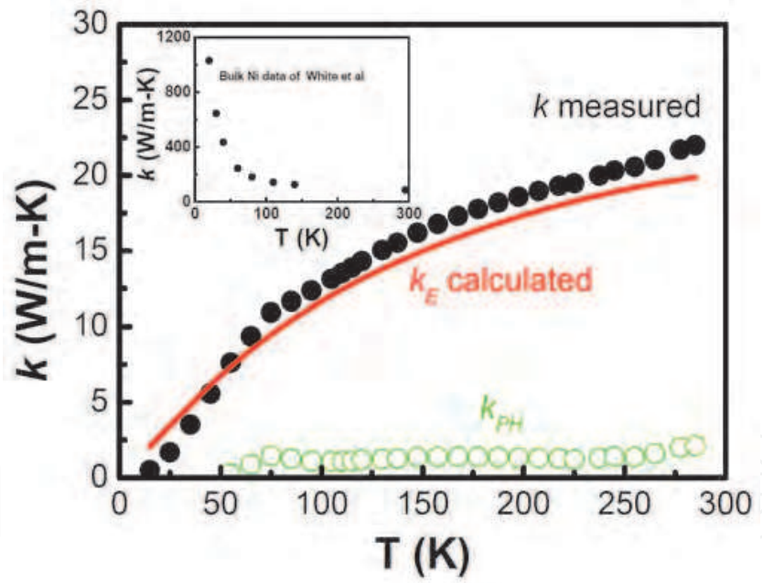

Fig. 21. The thermal conductivity $\kappa(T)$ of the Ni-NW (solid circles), the calculated κ_E (solid line) and the κ_{PH} (open circles). Inset: the thermal conductivity $\kappa(T)$ of the pure bulk Ni (White & Wood, 1959). (Reproduced with permission from Ou M. N. et al., *Appl. Phys. Lett.*, 92, 063101-063103. Copyright ©2008 from American Institute of Physics).

4. Conclusion

In summary, a couple of nanowire fabrication methods, that can efficiently control growth condition, sample composition, size/diameter, and crystallization of nanowires, are

introduced. Furthermore the morphology, microstructures and crystallization of nanowires are characterized by SEM, TEM, XRD and EDX. The techniques for measurements of Seebeck coefficient, electrical conductivity and thermal conductivity for either nanowires array or a single nanowire are also illustrated thoroughly. Some novel physical properties of nanowires are revealed by the measurements. A typical example of a single sagging Ni-NW was used to illustrate the specimen preparation and measurement setups. These innovative techniques of sample fabrication, characterization and measurements provide new strategies to understand the intrinsic properties of nanowires. Especially these knowledge and technologies are applicable to improve the thermoelectric efficiency of materials on renewable energy applications.

5. Acknowledgments

Financial supported by the National Science Council of the Republic of China (Grant No. NSC 99-2120-M-001-001) is greatly acknowledged. We deeply appreciate to all of our colleagues and collaborators, their names appear in the cited literatures. We would like to thank Mr. T. C. Hsiung and Ms. Candy I Chen Tsai for their important contributions to the research effort.

6. References

Allwood, D. A.; Xiong, G.; Faulkner, C. C.; Atkinson, D.; Petit, D. & Cowburn, R. P. (2005). Magnetic Domain-Wall Logic. *Science*, Vol. 309, pp. 1688-1692.

Andricacos, P. C.; Uzoh, C.; Dukovic, J. O.; Horkans, J. & Deligianni, H. (1998). Damascene Copper Electroplating for Chip Interconnections. *IBM J. Res. Dev.*, Vol. 42, pp.567-574.

Baily, S. A. & Emin, D. (2006). Transport Properties of Amorphous Antimony Telluride. *Phys. Re*v. B, Vol. 73, pp. 165211-165218.

Berman, R. (1976). *Thermal Conduction in Solids*. Oxford University Press. USA.

Bid, A.; Bora, A. & Raychaudhuri, A. K. (2006). Temperature Dependence of The Resistance of Metallic Nanowires of Diameter ≥ 15 nm: Applicability of Bloch-Gruneisen Theorem. *Phys. Rev.* B, Vol. 74, pp. 035426-035433.

Borca-Tasciuc, D. -A.; Chen, G.; Prieto, A.; Martin-Gonzalez, M. S.; Stacy, A.; Sands, T.; Ryan, M. A. & Fleurial, J. P. (2004). Thermal Properties of Electrodeposited Bismuth Telluride Nanowires Embedded in Amorphous Alumina. *Appl. Phys. Lett.,* Vol. 85, pp. 6001-6003.

Chen, C. L.; Chen, Y. Y.; Lin, S. J.; Ho, J. C.; Lee, P. C.; Chen, C. D. & Harutyunyan, S. R. (2010). Fabrication and Characterization of Electrodeposited Bismuth Telluride Films and Nanowires. J. Phys. Chem. C, Vol. 114, pp. 3385-3389.

Frase, H. & Fultz, B. (1998). Phonon in Nanocrystalline Ni_3Fe. *Phys. Rev.* B, Vol. 57, pp. 898-905.

Fultz, B.; Ahn, C. C.; Alp, E. E.; Sturhahn, W. & Toellner, T. S. (1997). Phonon in Nanocrystalline ^{57}Fe. *Phys. Rev. Lett.*, Vol. 79, pp. 937-940.

Ham, J.; Shim, W.; Kim, D. H.; Lee, S.; Roh, J.; Sohn, S. W.; Oh, K. H.; Voorhees, P. W. & Lee, W. (2009). Direct Growth of Compound Semiconductor Nanowires by On-Film Formation of Nanowires: Bismuth Telluride. *Nano Lett.*, Vol. 9, pp. 2867-2872.

Hicks, L. D. & Dresselhaus, M. S. (1993). Thermoelectric Figure of Merit of A One-Dimensional Conductor. *Phys. Rev*. B, Vol. 47, pp. 16631-16634.

Huang, Q.; Kellock, A. J. & Raoux, S. (2008). Electrodeposition of SbTe Phase-Change Alloys. *J. Electrochem. Soc.,* Vol. 155, pp. D104-109.

Jin, C.; Zhang, G.; Qian, T.; Li, X. & Yao, Z. (2005). Large-Area Sb_2Te_3 Nanowire Arrays. *J. Phys. Chem. B,* Vol. 109, pp. 1430-1432.

Leimkuhler, G.; Kerkamm, I. & Reineke-Koch, R. (2002). Electrodeposition of Antimony Telluride. *J. Electrochem. Soc.,* Vol. 149, pp. C474-478.

Li, D.; Wu, Y.; Kim, P.; Shi, L.; Yang, P. & Majumdar, A. (2003). Thermal Conductivity of Individual Silicon Nanowires. *Appl. Phys. Lett.,* Vol. 83, pp. 2934-2936.

Liu, K.; Nagodawithana, K.; Searson, P. C. & Chien, C. L. (1995). Perpendicular Giant Magnetoresistance of Multilayered Co/Cu Nanowires. *Phys. Rev*. B, Vol. 51, pp. 7381-7384.

Lu, L.; Yi, W. & Zhang, D. L. (2001). 3ω Method for Specific Heat and Thermal Conductivity Measurements. *Rev. Sci. Instrum*., Vol. 72, pp. 2996-3003.

Martin-Gonzlez, M. S.; Prieto, A. L.; Gronsky, R.; Sands, T.; Stacy, A. M. (2002). Insights Into The Electrodeposition of Bi_2Te_3. *J. Electrochem. Soc.,* Vol. 149, pp. C546-554.

Michel, S.; Diliberto, S.; Boulanger, C. & Bolle, B. (2006). Effect of Electrochemical Deposition Conditions on The Crystallographic Texture of Bismuth Telluride Alloys. *J. Cryst. Growth*, Vol. 296, pp. 227-233.

Osaka, T. (1999). Recent Development of Magnetic Recording Head Core Materials by Plating Method. *Electrochim. Acta*, Vol. 44, pp. 3885-3890.

Ou, M. N.; Harutyunyan, S. R.; Lai, S. J.; Chen, C. D.; Yang, T. J. & Chen, Y. Y. (2007). Thermal and Electrical Transport Properties of A Single Nickel Nanowire. *Physica Status Solidi* (b), Vol. 244, pp. 4512–4517.

Ou, M. N.; Yang, T. J.; Harutyunyan, S. R.; Chen, Y. Y.; Chen, C. D. & Lai, S. J. (2008). Electrical and Thermal Transport in Single Nickel Nanowire. *Appl. Phys. Lett*., Vol. 92, pp. 063101-063103.

Ou, M. N.; Yang, T. J. & Chen, Y. Y. (2009). Anisotropic Magnetism and Magnetoresistance in Iron Nanowire Arrays. *Chin. J. Phys.,* Vol. 47, pp. 848-853.

Reale, C. (1974). Conductivity Data for The Transition Metals Derived from Considerations on The Charge Transport in Thin Films. *J. Phys. F: Metal Phys.*, Vol. 4, pp. 2218-2222.

Reich, D. H.; Tanase, M.; Hultgren, A.; Bauer, L. A. & Chen, C. S. (2003). Biological Applications of Multifunctional Magnetic Nanowires. *J. Appl. Phys*., Vol. 93, pp. 7275-7280.

Rowe, D. M. (1995). *CRC Handbook of Thermoelectric.* CRC Press: New York.

Shim, W.; Ham, J.; Lee, K.; Jeung, W. Y.; Johnson, M. & Lee. W. (2009). On-Film Formation of Bi Nanowires with Extraordinary Electron Mobility. *Nano Lett*., Vol. 9, pp. 18-22.

Tritt, T. M. (1999). Thermoelectric Materials: Holey and Unholey Semiconductors. *Science,* Vol. *283*, pp. 804-805.

Tu, K. N. (1996). Cu/Sn Interfacial Reactions: Thin-Film Case Versus Bulk Case. *Mater. Chem. Phys*., Vol. 46, pp. 217-223.

Venkatasubramanian, R.; Siivola, E.; Colpitts, T. & O'Quinn, B. (2001). Thin-Film Thermoelectric Devices with High Room-Temperature Fgures of Merit. *Nature*, Vol. 413, pp. 597-602.

Weller, D. & Moser, A. (1999). Thermal Effect Limits in Ultrahigh-Density Magnetic Recording. *IEEE Trans. Magn.*, Vol. 35, pp. 4423-4439.

White, G. K. & Wood, S. B. (1959). Electrical and Thermal Resistivity of the Transition Elements at Low Temperatures. *Philos. Trans. R. Soc. London, Ser.* A, Vol. 251, pp. 273-302.

Yang, Y.; Zhu, J. G.; White, R. M. & Asheghi, J. (2006). Field-Dependent Thermal and Electrical Transports in Cu/CoFe Multilayer. *J. Appl. Phys.*, Vol. 99, pp. 063703-063707.

Zhang, X. Y.; Zhang, L. D.; Chen, W.; Meng, G. W.; Zheng, M. J. & Zhao, L. X. (2001). Electrochemical Fabrication of Highly Ordered Semiconductor and Metallic Nanowire Arrays. *Chem. Mater.*, Vol. 13, pp. 2511-2515.

Zhang, Q. G.; Cao, B. Y.; Zhang, X.; Fujii, M. & Takahashi, K. (2006). Influence of Grain Boundary Scattering on The Electrical and Thermal Conductivities of Polycrystalline Gold Nanofilms. Phys. Rev. B, Vol. 74, pp. 134109-134113.

Zhou, Z.; Uher, C.; Xu, D.; Johnson, W. L.; Gannon, W. & Aronson, M. C. (2006). On The Existence of Einstein Oscillators and Thermal Conductivity in Bulk Metallic Glass. Appl. Phys. Lett., Vol. 89, pp. 031924-031926.

Nanowires - Fundamental Research

Edited by Dr. Abbass Hashim

ISBN 978-953-307-327-9
Hard cover, 552 pages
Publisher InTech
Published online 19, July, 2011
Published in print edition July, 2011

Understanding and building up the foundation of nanowire concept is a high requirement and a bridge to new technologies. Any attempt in such direction is considered as one step forward in the challenge of advanced nanotechnology. In the last few years, InTech scientific publisher has been taking the initiative of helping worldwide scientists to share and improve the methods and the nanowire technology. This book is one of InTechâ€™s attempts to contribute to the promotion of this technology.

How to reference

In order to correctly reference this scholarly work, feel free to copy and paste the following:

Yang-Yuan Chen, Cheng-Lung Chen, Ping-Chung Lee and Min-Nan Ou (2011). Fabrication, Characterization and Thermal Properties of Nanowires, Nanowires - Fundamental Research, Dr. Abbass Hashim (Ed.), ISBN: 978-953-307-327-9, InTech, Available from: http://www.intechopen.com/books/nanowires-fundamental-research/fabrication-characterization-and-thermal-properties-of-nanowires

INTECH
open science | open minds

InTech Europe
University Campus STeP Ri
Slavka Krautzeka 83/A
51000 Rijeka, Croatia
Phone: +385 (51) 770 447
Fax: +385 (51) 686 166
www.intechopen.com

InTech China
Unit 405, Office Block, Hotel Equatorial Shanghai
No.65, Yan An Road (West), Shanghai, 200040, China
中国上海市延安西路65号上海国际贵都大饭店办公楼405单元
Phone: +86-21-62489820
Fax: +86-21-62489821

IntechOpen